SPE 59311

A Predictive Network Model for Three-Phase Flow in Porous Media
Thomas R. Lerdahl, SPE, Pål-Eric Øren, SPE, and Stig Bakke, Statoil Research Centre

Abstract
We reconstruct three-dimensional (3D) Berea sandstone samples by stochastically modeling the results of the main sandstone forming processes. The morphology of the reconstructed microstructure is compared quantitatively with a microtomography image of an actual sample of Berea sandstone. The comparison shows that the process based reconstruction adequately reproduces important intrinsic properties such as the local porosity distribution and the degree of connectivity. The reconstructed pore space is transformed into a pore network that is used directly as input to a network model. The model simulates two-phase flow and drainage dominated three-phase flow. Computed relative permeabilities for reconstructed Berea sandstone samples are compared with experimental data. The predicted relative permeability curves for both two-phase and three-phase flow compare favorably with the experimental results. Both the experiments and the simulations show that continuous oil layers present in the corners of gas invaded pores may allow low oil saturations to be reached during drainage dominated three-phase flow. However, the residual oil saturation and the oil permeability are strongly dependent on the saturation history.

Introduction
Three-phase flow in porous media is of great theoretical and practical interest in many fields of technology. Important industrial applications arise in enhanced oil recovery processes where gas is injected into reservoirs containing oil and water and in pollutant transport and cleanup. To understand and predict the fluid movement, accurate estimates of relative permeabilities are needed. In the case of two-phase flow, relative permeabilities are routinely measured experimentally, although they are often time consuming to obtain. Three-phase relative permeabilities, however, are both difficult and expensive to determine experimentally. Furthermore, it is impractical to measure relative permeabilities for the full range of possible saturation paths that may occur in three-phase flow. Three-phase behavior is therefore almost always estimated from two-phase data on the basis of empirical models. The models most often used are similar to the models first proposed by Stone [1,2] and later extended by others [3–6]. The empirical nature of these models constitutes a major deficiency in the present theory for three-phase flow in porous media.

In principle, it is not necessary to actually measure two-phase and three-phase relative permeability data since it is possible to determine these by appropriately averaging the equations describing the physical processes occurring on the pore-scale. This approach requires a detailed understanding of the pore-scale displacement mechanisms and a sufficient description of the pore space morphology. In recent years, our physical understanding of three-phase flow at the pore level has increased significantly [7–15]. This has lead to the development of network models for three-phase flow which predict macroscopic flow functions, such as relative permeability and capillary pressure, directly from a description of the pore structure and the displacement physics [16–21]. However, the difficulty in adequately describing the complex pore structure of real rocks has prevented these models from being used as predictive tools and no first principles predictions of three-phase relative permeabilities have yet been made [6].

Recently, Bakke and Øren [22] developed a process based reconstruction technique to generate a reliable 3D description of the pore space of actual sandstones. The technique utilizes petrographical information obtained from 2D thin section images to stochastically model the results of the main sandstone forming process – sedimentation, compaction, and diagenesis. Using this technique, they reconstructed Fontainebleau sandstone samples and found good agreement between predicted and measured absolute permeabilities and formation factors over a wide range of porosity [23]. Øren et.al. [24] applied the technique to reconstruct Bentheimer sandstone and successfully predicted two-phase relative permeabilities for both drainage and imbibition using network modeling techniques.

In the present work, we apply the technique to reconstruct 3D Berea sandstone samples. To assess the quality of the reconstruction, we compare quantitatively the morphology of the simulated pore structure with a microtomography image of an actual Berea sandstone sample. The permeability and formation factor of the sam-

ples are determined by solving the local partial differential equations which govern the transport phenomena. To predict relative permeabilities, the reconstructed pore space is transformed into a pore network that is used directly as input to a network model. Predicted two-phase and drainage dominated three-phase relative permeabilities are compared with the experimental data of Oak [25].

The rest of the paper is organized as follows: In Section 2 we briefly review the process based reconstruction technique and compare quantitatively various morphological and transport properties of a reconstructed Berea sample with those of a microtomography image of an actual Berea sample. Section 3 introduces the three-phase network model and describes the pore-scale displacement mechanisms on which the model is based. In Section 4, we compare the computed two-phase and three-phase relative permeabilities of the reconstructed samples to experimental data. Finally, Section 5 concludes the paper by summarizing our results.

Reconstructed Berea samples

A sandstone sample and its petrographical parameters are the end result of a series of complex geological and hydrodynamical processes. The detailed physics and chemistry of these processes are not fully understood and are the subject of much investigation. We thus emphasize that we do not try to model the formation of sandstones from first principles. Instead, we attempt to build sandstone models that are analogs of actual sandstones by stochastically modeling the *results* of the main sandstone forming processes: sedimentation, compaction, and diagenesis.

In short, sedimentation is modeled by sequentially depositing spherical quartz grains in a gravitational field. Each grain falls under the action of its own weight until it attains a stable position at a local or global minimum in potential energy. The resulting grainbed is compacted by shifting the vertical coordinate of every grain downwards by an amount that is proportional to the original vertical position. Quartz cement overgrowth is modeled by radially enlarging each grain. Authigenic clay growth is simulated by precipitating clay particles on the free mineral surface. The clay texture may be pore lining, pore filling, or pore bridging. Details about the sandstone reconstruction algorithm are described elsewhere [22–24].

Input data for the reconstruction are obtained from standard petrographical thin sections. They include porosity, the type and amount of cement and clay materials, grain size distribution, and visual estimates of the degree of compaction. Thin section analyses of Berea sandstone samples of different porosities reveal that they are made up of well sorted grains ranging in size from 70 to 400 μm [26]. The predominately quartz sand grains are cemented by quartz, dolomite, and clays. Quartz is the dominant
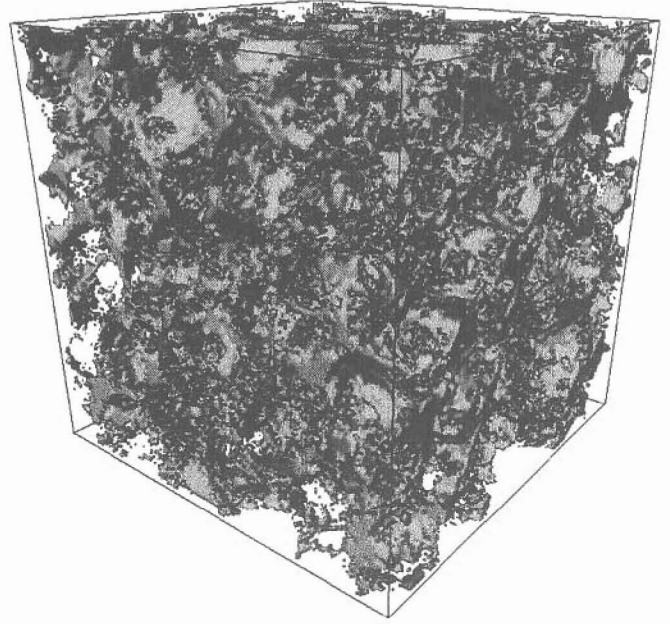

Fig. 1 – Image of the pore space in a 128^3 voxels subregion of the reconstructed sample PM3.

cementing material while the main clay component is pore filling kaolinite. The total clay content is roughly 7-9%. Based on the results from thin section analyses, we reconstructed four realizations of Berea sandstone (referred to as samples PM1 to PM4) by slightly varying the petrographical input parameters.

For each sample, a cubic subsample of size 300^3 voxels was extracted and used for data calculation. The resolution of each sample was 10 μm. In the resulting digitized samples, space can be divided into two disjoint phases (pore or matrix) by an indicator function Z such that

$$Z(\mathbf{x}) = \begin{cases} 1 & \text{if pore space at } \mathbf{x}, \\ 0 & \text{otherwise,} \end{cases} \quad (1)$$

where $\mathbf{x}$ denotes a lattice vector. Quartz cement and clays are here treated as being part of the matrix. The intergranular porosity is calculated from Z as the statistical average $\phi_M = \langle Z(\mathbf{x}) \rangle$. **Fig. 1** depicts a $128 \times 128 \times 128$ voxels subsample of the pore space of the process based model PM3. **Fig. 2** shows a microtomography image of the pore space of an actual Berea sample of almost identical porosity [27]. The sample has sidelength 1280 μm and a spatial resolution of 10 μm. It is abbreviated as sample CT in the following.

Visual inspection of Figs. 1 and 2 reveals that the reconstruction is not perfect. Although the reconstructed microstructure is not substantially different from the reference sample CT, it differs visibly in the shape of the grains.
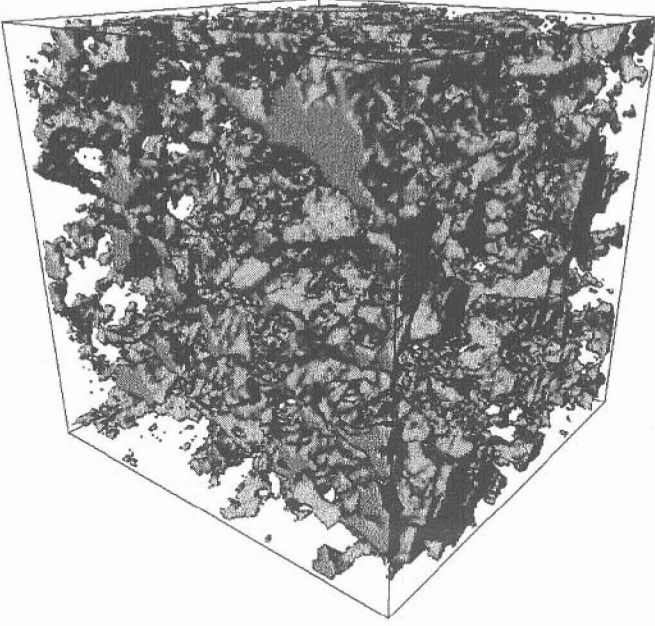
Fig. 2 – Microtomography image of the pore space of Berea sandstone (sample CT).

It also appears to be more homogenous than the actual sandstone. However, it is important to realize that average properties of different media may agree closely even if visual appearances suggest otherwise. Consequently, to judge if a reconstruction can be deemed successful, we need to quantitatively compare important morphological and transport properties of the samples.

Two-point correlation functions. In contrast to statistical based reconstruction methods [28–30], our process based reconstruction technique is not based on matching the two-point correlation function of the actual sample. It is thus unclear to which extent the process based reconstruction is able to reproduce such information. The two-point correlation function is calculated from the indicator Z as the statistical average

$$C_2(\mathbf{u}) = \frac{\langle (Z(\mathbf{x}) - \phi_M)(Z(\mathbf{x} + \mathbf{u}) - \phi_M) \rangle}{\phi_M(1 - \phi_M)}. \quad (2)$$

$C_2(\mathbf{u})$ measures the probability of finding the two end points of a segment of length $\mathbf{u}$ within the same phase, pore space or matrix. Correlation functions for line segments parallel to the x-, y-, and z-direction are denoted as $C_{2x}(L)$, $C_{2y}(L)$, and $C_{2z}(L)$, respectively, where $L = \|\mathbf{u}\|$. For an isotropic medium, these three functions must coincide with the directionally averaged correlation function $C_2 = (C_{2x} + C_{2y} + C_{2z})/3$. The specific internal surface, S, of the digitized samples is extracted from the initial slope
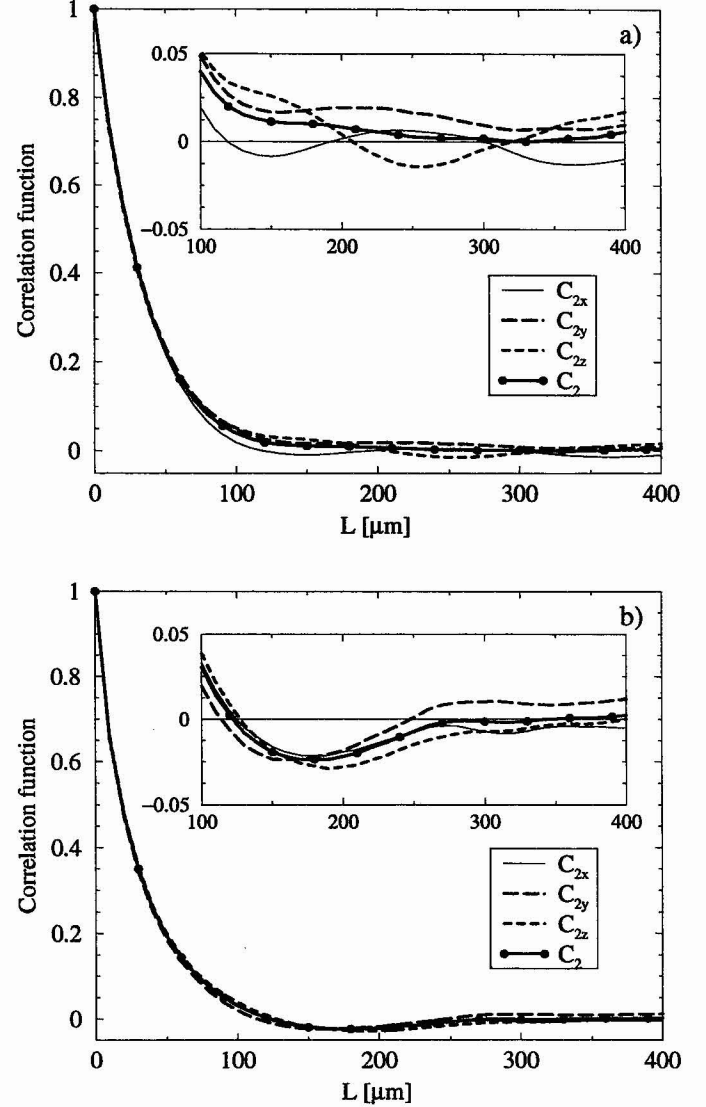
Fig. 3 – Two-point correlation functions of a) sample CT, and b) sample PM3.

of the two-point correlation function as [30]

$$S = -6\phi_M(1 - \phi_M) \left. \frac{dC_2(L)}{dL} \right|_{L=0}. \quad (3)$$

Two-point correlation functions of the samples PM3 and CT are shown in **Fig. 3**. Overall, the correlation functions of the reconstructed sample is quite similar to those of the microtomography image. Deviations between C_{2x}, C_{2y}, and C_{2z} are relatively small, indicating a high degree of isotropy in both samples. The initial decay of the averaged correlation function is slightly steeper for sample PM3 than for sample CT. This can be seen by comparing the correlation length, $L_C = -1/(dC_2/dL)_{L=0}$ of the two samples, cf. **Table 1**. The shorter correlation length for

	ϕ_M [%]	S [μm^{-1}]	L_C [μm]	L_μ [μm]	L^* [μm]
CT	17.8	0.0225	38	63	260
PM3	17.9	0.0304	29	57	250

Table 1. Properties of samples CT and PM3, derived from the indicator function Z.

sample PM3 (29 μm vs. 38 μm) indicates that it is more homogeneous than sample CT.

Local porosity distributions. Local porosity distributions [31–34], $\mu(\phi, L)$, are obtained from the indicator Z in the following way: Let $\phi(\mathbf{x}, L) = \langle Z(\mathbf{x}) \rangle_{\mathcal{M}}$ denote the porosity of a cubic measurement cell $\mathcal{M}(\mathbf{x}, L)$ of sidelength L centered at position $\mathbf{x}$, then

$$\mu(\phi_k, L) = \frac{1}{m} \sum_{\mathbf{x}} \delta(\phi_k - \phi(\mathbf{x}, L)) \qquad (4)$$

with the indicator

$$\delta(\phi_k - \phi(\mathbf{x}, L)) = \begin{cases} 1 & \text{if } |\phi_k - \phi(\mathbf{x}, L)| \leq \Delta\phi \\ 0 & \text{otherwise} \end{cases} \qquad (5)$$

$\mu(\phi, L)$ measures the empirical probability of finding the local porosity $\phi(\mathbf{x}, L)$ in the range $\phi_k \pm \Delta\phi$, with $\phi_{k+1} - \phi_k = 2\Delta\phi$. In Eq. 4, m denotes the total number of measurement cells. Ideally, the measurement cells should not overlap, but in practice this can not be done because of poor statistics. The results presented below were obtained by placing $\mathcal{M}(\mathbf{x}, L)$ on all voxels which are at least a distance $L/2$ from the boundaries of the sample.

Fig. 4 displays local porosity distributions at different length scales for the samples CT and PM3. They are compared to binomial distributions

$$B_{n,\phi_M}(k) = \binom{n}{k} \phi_M^k (1 - \phi_M)^{n-k}, \qquad (6)$$

plotted as a function of $\phi_k = k/n$, $k = 0, \ldots, n$. Since $B_{n,\phi_M}(k)$ is the probability of finding k of n *statistically independent* events to give the same result (of elementary probability ϕ_M), we can derive a correlation length L_μ from the relation $(L/L_\mu)^3 = n^*$, where n^* is the value of n for which the deviation $\sum_k (\mu(\phi_k, L) - B_{n,\phi_M}(k))^2$ is minimal.

The slightly smaller value of L_μ for sample PM3 (57 μm vs. 63 μm) again suggests that sample PM3 is more homogeneous than sample CT. Also included in Table 1 is the length scale L^* [33], defined as the smallest L for which all measurement cells contain both matrix and pore space, such that $\mu(\phi = 0, L^*) = \mu(\phi = 1, L^*) = 0$. L^* gives the sidelength of the largest cube that can be fit into
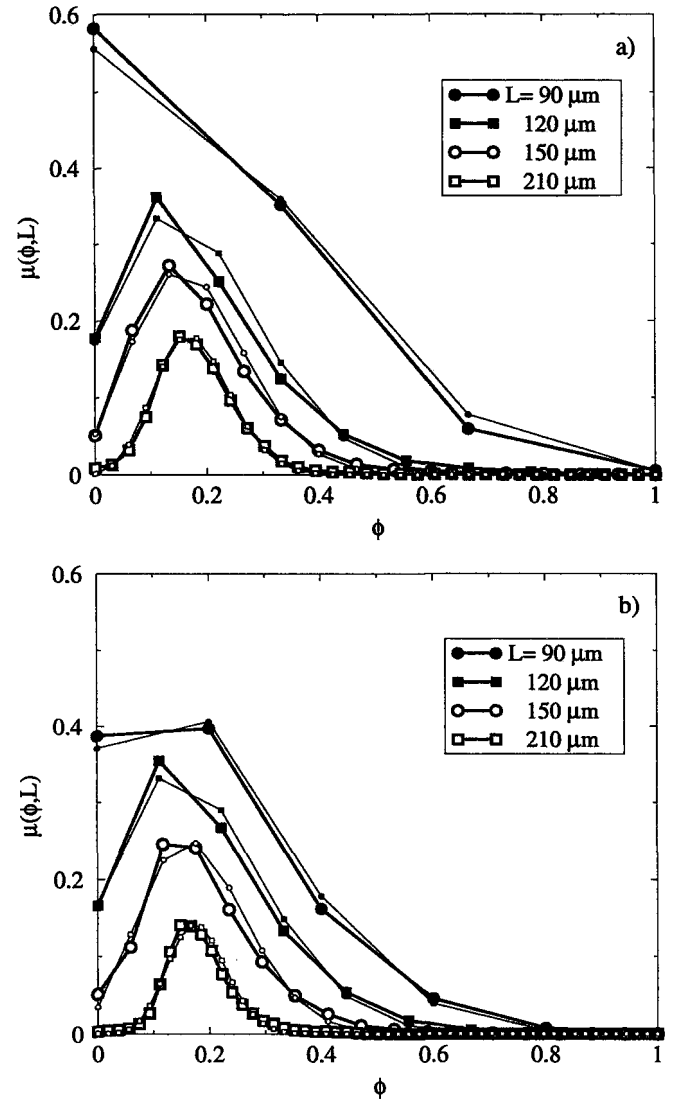
Fig. 4 – Local porosity distributions $\mu(\phi, L)$ (thick lines) and best fit binomial B_{n^*, ϕ_M} (thin lines) for a) sample CT and b) sample PM3.

matrix space and can be viewed as a measure of the size of the largest grain. Table 1 shows that sample CT has a larger L^* than sample PM3 (260 μm vs. 250 μm).

Local percolation probabilities. While the correlation functions and the local porosity distributions quantify geometric features of the pore space, local percolation probabilities [31–34] provide a quantitative characterization of its connectivity. For our purpose, we introduce $P_i(L)$ as the total fraction of all measurement cells $\mathcal{M}(\mathbf{x}, L)$ that percolate in the i-direction:

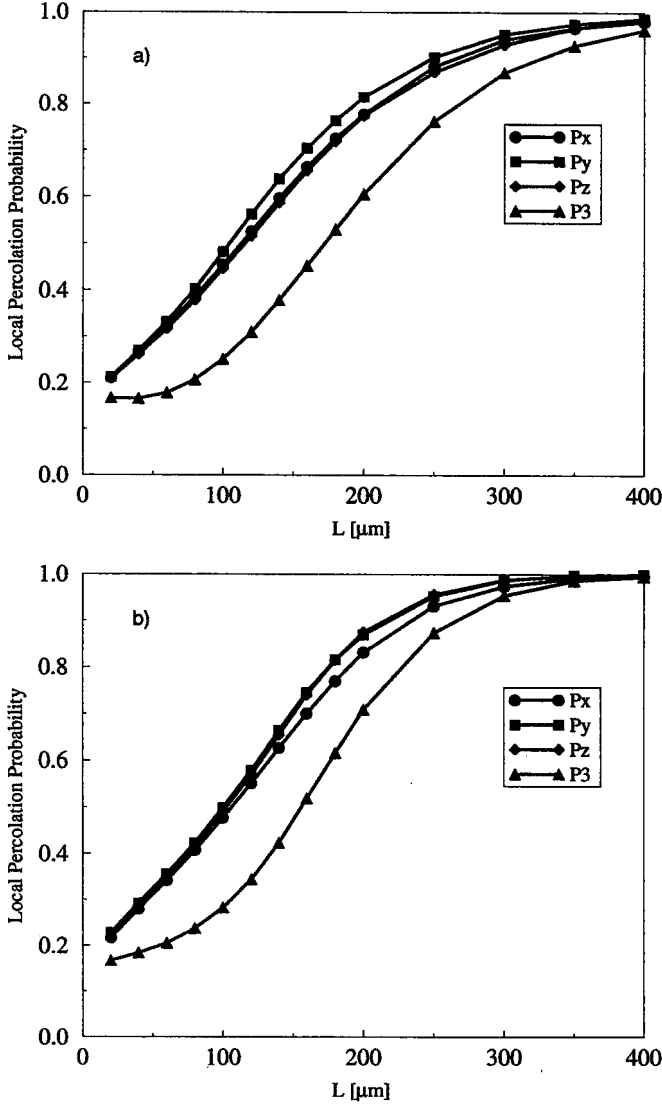$$P_i(L) = \frac{1}{m} \sum_{\mathbf{x}} \Lambda_i(\mathbf{x}, L) \qquad (7)$$

Fig. 5 – Average percolation probabilities $P_i(L)$ of a) sample CT and b) sample PM3 for $i = x, y, z$, and 3.

with the indicator

$$\Lambda_i(\mathbf{x}, L) = \begin{cases} 1 & \text{if } \mathcal{M}(\mathbf{x},\text{L}) \text{ percolates} \\ 0 & \text{otherwise} \end{cases} \tag{8}$$

A measurement cell is said to percolate in the i-direction if there exists a continuous path inside the pore space that connects the inlet and outlet face of $\mathcal{M}$, chosen perpendicular to the direction i.

Fig. 5 displays the local percolation probabilities as a function of L for the samples CT and PM3. P_3 denotes the fraction of cells that percolates in all three principal directions. Although the P_i-functions of sample PM3 rise more rapidly than those of sample CT, the connectivities of the two samples appear to be quite similar. Both samples

are fairly isotropic in their connectivities because the P_x-, P_y-, and P_z-functions all fall nearly on top of each other. Sample CT has a slightly higher connectivity in the y-direction than in the x- and z-directions while sample PM3 has a slightly lower connectivity in the x-direction than in the other directions.

In summary, the process based model PM3 adequately reproduces the two-point correlation function and the local porosity distributions of the reference sample CT. However, the shorter correlation lengths suggest that the process based reconstruction is more homogenous than sample CT. Most importantly, the 3D connectivity properties of the simulated sample appears to be similar to that of the actual sample. This is encouraging and suggests that the process based reconstruction is able to reproduce intrinsic 3D connectivity properties that are important for transport. A similar result was found in an earlier study on Fontainebleau sandstone [23]. The remainder of this section is devoted to the calculation of single phase transport properties on the digitized samples.

Formation Factor. The directional formation factor, F_i, is defined as the inverse of the macroscopic electrical conductivity, σ_i, of a porous medium in a given i-direction:

$$F_i = \frac{\sigma_w}{\sigma_i}, \tag{9}$$

where σ_w is the bulk electrical conductivity of the fluid that fills the pore space. We compute σ_i for the three principal directions from a linear relation between the total electrical flux, Q_i, and the applied potential gradient, $(\Phi_I - \Phi_O)/L$:

$$Q_i = -\sigma_i \frac{(\Phi_I - \Phi_O)}{L} A. \tag{10}$$

The potential Φ_I is applied to an inlet face, Ω_I, of area A, and the potential Φ_O to an outlet face, Ω_O, separated from Ω_I by a distance L. To obtain the electrical flux, we solve the Laplace equation

$$\nabla \cdot (\sigma \nabla \Phi) = 0, \tag{11}$$

where the microscopic fluid conductivity is distributed as $\sigma(\mathbf{x}) = \sigma_w Z(\mathbf{x})$, i.e. we assume the matrix to be insulating. Consequently, the gradient of the electrical potential Φ must vanish at the fluid/solid boundary, S, i.e. $\nabla \Phi \cdot d\mathbf{S} = 0$, where $d\mathbf{S}$ denotes the outward normal to dS. Details of the solution strategy are described by Øren and Bakke [23]. The electric field is calculated from Φ by $\mathbf{E} = -\sigma \nabla \Phi$, and the total electrical flux through Ω_I is

$$Q_i = \int_{\Omega_I} \mathbf{n}\,\mathbf{E}\, d\Omega_I. \tag{12}$$

	CT	PM1	PM2	PM3	PM4
$\phi_t[\%]$	–	25.6	26.4	23.8	24.0
$\phi_M[\%]$	17.8	19.4	20.0	17.9	18.2
F_x	46.8	35.9	34.4	43.0	42.3
F_y	38.5	33.1	33.4	40.3	44.9
F_z	40.4	32.3	31.5	40.0	38.9
F	41.6	33.7	33.1	41.0	41.9
k_x [mD]	585	530	506	418	394
k_y [mD]	871	582	478	478	353
k_z [mD]	817	749	620	490	523
k [mD]	758	620	543	462	423

Table 2. Porosities and calculated transport properties for all samples. CT: microtomography image, PM1 to PM4: different realizations of the process-based reconstructions.

An average formation factor, F, is obtained from the harmonic mean $3/F = (1/F_x + 1/F_y + 1/F_z)$. We note that F is a scale-invariant quantity. If we uniformly increase or decrease the size of the pores and the matrix, leaving the porosity unchanged, the value of F is unaffected.

Absolute Permeability. Absolute directional permeability, k_i, is defined by Darcy's law

$$Q_i = \frac{k_i}{\mu} \frac{(p_I - p_O)}{L} A \,, \tag{13}$$

where Q_i is the macroscopic flux obtained from applying a macroscopic pressure gradient $(p_I - p_O)/L$ in a direction i. To calculate the directional permeabilities, we assume the flow to be governed by the steady state Stokes equations for an incompressible Newtonian fluid of viscosity μ

$$\mu\nabla^2\mathbf{v} = \nabla p \,, \tag{14}$$

$$\nabla \cdot \mathbf{v} = 0 \,, \tag{15}$$

subject to a no-flow boundary condition ($\mathbf{v} = 0$) on the fluid/solid boundary. We employ the artificial compressibility scheme [35] to solve this partial differential equation on the digitized samples. From the resulting velocity field, the macroscopic flux Q_i is obtained by integrating $\mathbf{v}$ over the inlet area. A directionally averaged permeability is defined as the arithmetic mean $k = (k_x + k_y + k_z)/3$.

Calculated values for the formation factor and the absolute permeability of all the samples are summarized in **Table 2**. The directionally averaged permeability of the four reconstructions ranges from 423 mD to 620 mD while the averaged permeability of sample CT is 758 mD. Compared to experimental measurements on Berea samples of similar porosity, the computed permeabilities appear to be too low [26]. This, however, is not surprising since the finite resolution of the models does not allow an accurate representation of the smaller pores. This also holds for the

microtomography image which has the same resolution as the reconstructed samples.

Both samples CT and PM3 are slightly anisotropic in their transport properties. Sample CT has a higher permeability and electrical conductivity in the y-direction than in the x- and z-directions while the reconstructed sample has a higher permeability and conductivity in the z-direction. The small anisotropy of sample PM3 (as well as the other reconstructions) is mainly attributed to the anisotropic compaction process which causes the connectivity in the horizontal x- and y-directions to decrease more rapidly than in the vertical z-direction [22].

The directionally averaged formation factors for samples PM3 and CT are almost identical (41.0 vs. 41.6). This suggests that the two samples have very similar tortuosity values since the porosities of the samples are almost identical. The directionally averaged permeabilities, however, differ by roughly 40%. This is a bit surprising considering the close agreement between the computed formation factors. However, while F is scale-invariant and depends only on the tortuosity (and porosity), k depends both on the tortuosity and on the absolute dimensions of the pores. The smaller permeability of sample PM3 suggests that the average pore size of the model is less than that of the microtomography image. This may also be inferred from the fact that sample CT has a larger L^* (i.e. grain size) than sample PM3. Generally, however, we find the agreement between the computed transport properties of the two samples quite encouraging.

The Multiphase Network Models
Although it is possible to perform multiphase flow simulations directly on the reconstructed microstructure, either by numerically solving the Navier Stokes equations or by applying a Lattice-Boltzmann simulation [36], it can only be done at considerable computational expense. It is therefore convenient to construct a pore network that replicates the main features of the pore space that are relevant to multiphase flow. The transformation of the reconstructed pore space into a pore network representation has been described in detail previously [22,24].

In short, it consists of first constructing the skeleton or line representation of the pore space. The skeleton provides information about the local connectivity or coordination number of every node or pore body in the network. With the mathematical skeleton as basis, we measure directly the main topological and geometrical properties of every node and link in the network. Briefly, each node/link I is assumed to have a simple cross-sectional shape (triangle, square, or circle), described by an inscribed radius, R_I, and corner half angles, $\beta_{I,j}$, as depicted in **Fig. 6 (a)**. Additional key parameters are the spacing between the nodes and the intergranular and clay associated pore

volumes, $V_{M,I}$ and $V_{m,I}$, of each node/link. The entire network is contained in a box of volume V_t, and connected to inlet and outlet nodes that serve as fluid reservoirs for injection and withdrawal of the fluids. The total porosity of a network is calculated from

$$\phi_t \, V_t = \sum_I (V_{M,I} + V_{m,I}) \,, \qquad (16)$$

where the sum extends over all nodes and links. For the reconstructed Berea samples, the total porosity is included in Table 2. We emphasize that we invoke no *a priori* assumptions about the network properties such as pore size distribution or coordination number. All the properties are determined directly from the reconstructed pore space. Further details are given in Øren *et.al.* [24].

In all the flow simulations we assume that capillary forces dominate at the pore-scale. This is a reasonable assumptions for capillary numbers in the range 10^{-6} and lower. Most corefloods are performed with capillary numbers in the range 10^{-5} to 10^{-8}. The assumption of capillary dominated flow is thus acceptable for low rate core floods as well as most reservoir displacements. The network model used here for simulating two-phase drainage and imbibition displacements is identical to that described in detail previously [24]. A discussion of displacement mechanisms, threshold capillary pressures, and the computation of hydraulic conductances and relative permeabilities are given in Ref. [24]. The remainder of this section is devoted to a description of the three-phase network model.

Three-phase model. The three-phase network model is currently limited to drainage dominated three-phase flow in water wet porous media. The model is based on the pore-scale displacement mechanisms observed in micromodel experiments, described in detail by Øren and Pinczewski [8,10,17]. Here we briefly introduce those concepts that are necessary for defining our network model.

Fluid configurations. When a porous medium is occupied by three immiscible fluids (gas, oil, and water), the static equilibrium pore-scale distribution of the fluids is determined by wettability, capillary pressure, and the spreading behavior of the fluids. For a water wet medium, water (w) is the wetting phase, gas (g) is the non-wetting phase, and oil (o) is the intermediate phase. Capillary pressure dictates that the wetting phase preferentially occupies the smaller pores and the corners of non-wetting or intermediate phase filled pores (cf. Fig. 6).

For a water filled link/node I (Fig. 6 (a)) , the water, oil, and gas saturations are

$$S_{w,I} = 1 \,, \quad S_{o,I} = 0 \,, \quad S_{g,I} = 0 \,, \qquad (17)$$

while the conductances to water, oil, and gas are

$$\sigma_{w,I} = \widetilde{\sigma}_{w,I} \,, \quad \sigma_{o,I} = 0 \,, \quad \sigma_{g,I} = 0 \,. \qquad (18)$$

where

$$\widetilde{\sigma}_{w,I} = \frac{3 \, R_I^2 \, A_{t,I}}{20 \, \mu_w} \,, \qquad (19)$$

is the single phase conductance of a triangular node/link I and $A_{t,I}$ is the cross-sectional area [24].

In regions of the pore space occupied by the wetting phase and only one of the non-wetting phases (gas or oil), the distribution of the two fluids is identical to that in a two-phase system (Fig. 6 (b) and (c)). Fig. 6 (b) depicts a corner of an oil filled node/link. The radius of the oil-water interface is given by

$$r_{w,I} = \frac{\gamma_{ow}}{P_{cow,I}}, \qquad (20)$$

where γ_{ow} and $P_{cow,I}$ are the oil-water interfacial tension and prevailing capillary pressure, respectively. The equilibrium oil-water-solid contact angle, θ_{ow}, is zero, since we assume strongly wetting conditions. The water occupied cross-sectional area in a corner j of an oil filled node/link I, $A_{w,I,j}$, can be calculated from elementary geometry [24]. Summing over corners, we assign water, oil, and gas saturations to an oil filled node/link by

$$S_{w,I} = \sum_j \frac{A_{w,I,j}}{A_{t,I}}, \quad S_{o,I} = 1 - S_{w,I}, \quad S_{g,I} = 0. \qquad (21)$$

Phase conductances to water, oil, and gas are

$$\sigma_{w,I} = \sum_j \sigma_{w,I,j}, \quad \sigma_{o,I} = S_{o,I} \, \widetilde{\sigma}_{o,I}, \quad \sigma_{g,I} = 0, \qquad (22)$$

with

$$\sigma_{w,I,j} = \frac{r_{w,I}^2 A_{w,I,j}}{b_{w,I,j} \, \mu_w}, \qquad (23)$$

where b_w is a dimensionless flow resistance factor which is obtained from numerical solutions of the corresponding corner flow problem [37,24].

Similarly, in the corners of a gas occupied node/link (Fig. 6 (c)), we find a gas-water interface with radius $r_{w,I} = \gamma_{gw} / P_{cgw,I}$, where γ_{gw} and $P_{cgw,I}$ are the gas-water interfacial tension and the prevailing capillary pressure, respectively. Again, the equilibrium gas-water contact angle, θ_{gw}, is zero. Phase saturations and phase conductances are again calculated from Eqs. (21 - 23) by interchanging the subscripts o and g.

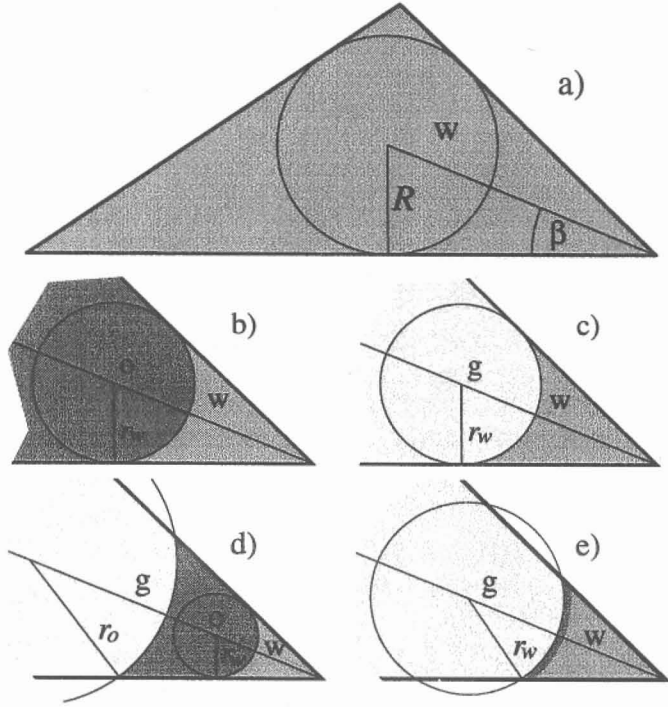However, there are two more possible corner configurations for a gas filled node/link: If the node/link was pre-

Fig. 6 – (a) Geometric concept for nodes/links and (b-e) equilibrium fluid configurations in a corner of a node/link. See the text for a discussion.

viously filled with oil, small amounts of oil may reside in the corners, as discussed in Refs. [10,11]. In this case, there exist a gas-oil interface with radius $r_{o,I} = \gamma_{go}/P_{cgo,I}$ and contact angle θ_{go} in addition to the oil-water interface of radius $r_{w,I} = \gamma_{ow}/P_{cow,I}$. The gas-oil contact angle is given by

$$\cos\theta_{go} = 1 + \frac{C}{\gamma_{go}}, \qquad (24)$$

where

$$C = \gamma_{gw} - (\gamma_{go} + \gamma_{ow}) \qquad (25)$$

is the spreading coefficient. Summing over all the corners, we assign water, oil, and gas saturations in this case by

$$S_{w,I} = \sum_j \frac{A_{w,I,j}}{A_{t,I}}, \quad S_{o,I} = \sum_j \frac{A_{o,I,j}}{A_{t,I}},$$

$$S_{g,I} = 1 - S_{o,I} - S_{w,I}. \qquad (26)$$

In a similar fashion, phase conductances are obtained from

$$\sigma_{w,I} = \sum_j \sigma_{w,I,j}, \quad \sigma_{o,I} = \sum_j \sigma_{o,I,j},$$

$$\sigma_{g,I} = S_{g,I}\,\tilde{\sigma}_{g,I} \qquad (27)$$

The existence of such oil layers in corners is connected

to a stability criterion: Increasing P_{cgo} or decreasing P_{cow} will move the gas-oil and the oil-water interfaces closer to each other and the oil layer thins. At a critical capillary pressure (which depends on the corner geometry and the spreading coefficient) the two interfaces meet and the oil layer collapses [38]. In a negative spreading system ($C < 0$), such a layer collapse results in a fluid configuration as sketched in Fig. 6 (c). In a positive spreading system ($C > 0$), a thin film of oil will always exist between the gas and the water phase, as illustrated in Fig. 6 (d). Such oil films reduce the gas-water interfacial tension to an equilibrium value, γ_{gw}^e, such that the equilibrium spreading coefficient

$$C^e = \gamma_{gw}^e - (\gamma_{go} + \gamma_{ow}) \leq 0 \qquad (28)$$

The equilibrium gas-oil contact angle is still given by Eq. (24), with C^e replacing C. Phase saturations and conductances for this fluid configuration are thus given by Eqs. (21 - 23), interchanging the subscripts o and g.

From a given equilibrium fluid distribution in the network, macroscopic phase saturations are obtained by volume averaging the phase saturations in all nodes and links through

$$S_w \phi_t V_b = \sum_i (S_{w,I} V_{M,I} + V_{m,I}),$$

$$S_o \phi_t V_b = \sum_i S_{o,I} V_{M,I}, \quad S_g = 1 - S_o - S_w. \qquad (29)$$

That is, the clay associated pore volumes (i.e. microporosity) is assumed to be water saturated and impermeable.

For laminar flow, the flow rate of phase n between two connecting nodes I and J in the network is given by

$$q_{n,IJ} = \frac{\langle \sigma_{n,IJ} \rangle}{L_{IJ}} (p_{n,I} - p_{n,J}) \qquad (30)$$

where L_{IJ} is the spacing between the pore body centers. The effective conductance $\langle \sigma_{n,IJ} \rangle$ is assumed to be the harmonic mean of the throat and the two pore body conductances. Phase permeabilities, k_n, are obtained by solving the Kirchhoff equation

$$\sum_J q_{n,IJ} = 0 \quad \forall I, \qquad (31)$$

with fixed pressure on specified inlet and outlet nodes. The sum of flow rates through the inlet nodes determines the macroscopic flow rate, Q_n, to be inserted into Darcy's law. Phase relative permeabilities are then calculated as $k_{rn} = k_n/k$.

Displacements events. In the absence of viscous effects, fluid displacement proceeds through a series of equilibrium configurations with respect to capillary and buoyancy forces. The three-phase displacements of interest in

the present study all involve the injection of gas into a pore network that initially contains only water and oil. Although regions of the network may be occupied by one, two, or all three fluids simultaneously, individual displacement events all involve an invasion of a pore throat or pore body by a two-phase interface. Displacements in three-phase flow may thus be described by a simple generalization of well understood two-phase displacements by including double displacements and film flow of the intermediate oil phase [10,17,19].

The following displacements may occur during drainage dominated three-phase flow in any node/link I of the network which is adjacent to a link/node K that is filled with invading gas:

DW (direct water drainage): Invading gas displaces water, which is recovered at the outlet.

DO (direct oil drainage): Invading gas displaces oil, which is recovered at the outlet.

DD (double drainage): Invading gas displaces trapped oil. The trapped oil, in turn, displaces water in a link/node J adjacent to the cluster of trapped oil. The displaced water is recovered at the outlet.

Note that DW- and DO-events require the displaced phase to be connected to the outlet. The wetting phase is hydraulically connected throughout the network and flows away from the invasion site to the outlet through interconnected water filled pores (bulk flow), through wetting films in the corners (film flow), or a combination of both. The manner in which the oil flows depends on the spreading behavior. If oil layers exist, oil flows in a manner exactly analogous to that of the wetting phase with oil layers connecting regions of bulk oil. In the absence of oil layers, oil flows in a manner similar to that of the gas, i.e., by bulk flow. DD-events allow the mobilization of trapped oil and subsequent coalescence of oil clusters. If no oil layers are present, both DD- and DO-events may result in breakup and trapping of oil clusters [10]. Oil is considered to be trapped when it is completely 'surrounded' by gas.

Associated with each of the above displacements is a threshold gas-water capillary pressure, P_{ct}. Among all the possible events, the one with the lowest threshold capillary pressure will be performed. If necessary, this is accommodated by an increase in the invading gas-water capillary pressure ($P_c^+ = \max(P_c, P_{ct})$). In drainage dominated three-phase flow, only piston-type displacements occur, and the threshold capillary pressure is given by

$$P_{ct} = \begin{cases} P_{ctgw,I} & \text{(for DW)} \\ P_{ctgo,I} + P_{cow,I} & \text{(for DO)} \\ P_{ctgo,I} + P_{Cow,J}^+ & \text{(for DD)} \end{cases} \quad (32)$$

	gas-water	gas-oil	oil-water
γ [mN/m]	55	20	30
θ_r [degrees]	0	0	0
θ_a [degrees]	0–10	0–10	10–30

Table 3. Interfacial tensions and contact angles used in the multiphase flow simulations.

where $P_{Cow,J}^+ = \max(P_{Cow,J}, P_{ctow,J})$ denotes the oil-water capillary pressure after the DD-event. The threshold capillary pressure for a piston type displacement in a node/link I is given by [24]

$$P_{ctnm,I} = \frac{(1 + 2\sqrt{\pi G_I})}{R_I} \gamma_{nm} \cos(\theta_{nm}) \quad (33)$$
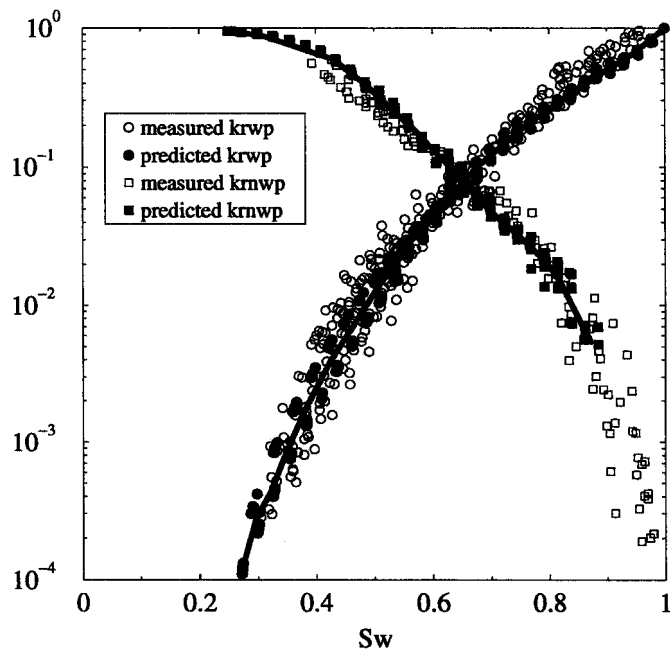
where G_I is a dimensionless shape factor which describes the cross-sectional shape of the node/link [24].

Results and Discussion

In a pioneering experimental work, Oak [25] collected approximately 1800 values of two-phase and three-phase relative permeabilities from carefully conducted steady state experiments on three samples of water wet Berea sandstone. The samples had permeabilities k ≈ 200 mD, 800 mD, and 1000 mD. The porosities of the samples were not reported. The fluids used were water, mineral oil or dodecane as the oil phase, and nitrogen as the gas phase. Unfortunately, Oak did not report values for the interfacial tensions or the contact angles. It was thus necessary to estimate these values, cf. **Table 3**.

The estimated interfacial tensions imply that we have a positive spreading system. This is consistent with the fact that the measured drainage oil relative permeabilities display a quadratic behavior (i.e. $k_{ro} \propto S_o^2$) at low oil saturations [6]. In all the drainage displacements, we assumed a receding contact angle $\theta_r = 0°$. To account for contact angle hysteresis, the advancing contact angle θ_a for oil-water imbibition was randomly distributed between 10° and 30°. Furthermore, to account for the fact that gas is a more strongly non-wetting phase than oil, θ_a for gas-liquid imbibition was randomly distributed between 0° and 10°. These values are consistent with a water wet system and are in agreement with contact angle measurements on quartz [39].

According to Oak, the low permeability sample displayed a different behavior than the two high permeable cores. Because of the low resolution (10 μm), our reconstructions are believed to be more representative of the high permeable cores than the low permeability one. In the following, we therefore compare our calculated two-phase and three-phase relative permeabilities to Oak's data for the two high permeable cores.
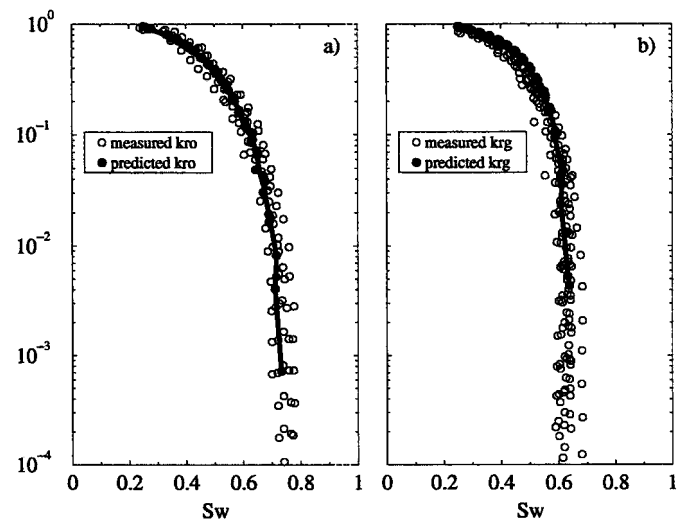
Fig. 8 — Predicted vs. measured non-wetting phase relative permeabilities for imbibition. (a) oil-water and (b) gas-oil/gas-water displacement.

Fig. 7 — Predicted vs. measured two-phase relative permeabilities. wetting phase: drainage and imbibition; non-wetting phase; drainage only. The experimental data for the non-wetting phase is for gas-liquid drainage.

Two-phase predictions. Oak divides the two-phase relative permeability data for the two high permeable cores into five groups:

1. wetting phase relative permeability,

2. drainage oil relative permeability,

3. drainage gas relative permeability,

4. imbibition oil relative permeability,

5. imbibition gas relative permeability.

The computed two-phase relative permeabilities are compared with the experimental data of Oak in **Figs. 7 and 8.** In all the plots, the open symbols are Oak's data, the filled symbols are the predicted data (for all the realizations), and the solid line is the average predicted relative permeability. Fig. 7 shows that the predicted wetting phase relative permeability agrees very well with the experimental data (Group 1). As expected for water wet systems, there is little hysteresis between drainage and imbibition wetting phase relative permeability. The experimental value of the irreducible water saturation, $Sw_{irr} \approx 0.27$, agrees well with the predicted value, $Sw_{irr} \approx 0.25$. Most of the simulated irreducible water saturation is located in the microporosity which is assumed to be impermeable.

In Oak's experiments, the drainage oil relative permeability (Group 2) was different (larger) than the drainage

gas relative permeability (Group 3). This disagrees with the commonly accepted view that two-phase drainage relative permeabilities for different fluid pairs are the same in strongly wetted porous media. Oak does not offer an explanation as to why they are different. The simulated drainage relative permeabilities were the same for all three fluid pairs and are shown in Fig. 7. They are compared to the experimental drainage gas relative permeabilities (Group 3). The predicted relative permeabilities agree reasonably well with the experimental data. Note that Oak's data contain gas relative permeabilities up to very high water saturations, while our predictions yield non-zero relative permeability only below $Sw \approx 0.9$. This is mainly due to the small size of the reconstructed samples (i.e. percolation threshold phenomena).

In Fig. 8 we compare predicted and measured imbibition relative permeabilities. Fig. 8 (a) shows the oil relative permeability (Group 4) while the gas relative permeability (Group 5) is depicted in Fig. 8 (b). Again, we find good agreement between measured and predicted results, including values of the residual non-wetting phase saturation. The difference in the simulated oil and gas imbibition relative permeabilities is due to the small difference in the advancing contact angle. This suggests that the balance between snap-off and piston type displacement in the high permeability samples is sensitive to small variations in the contact angle. This would not be the case for low permeability media where the aspect ratio (ratio of pore body size to throat size) is larger and snap-off is the preferred displacement event. In his experiments, Oak noted that the imbibition oil and gas relative permeabilities were the same in the low permeable sample.
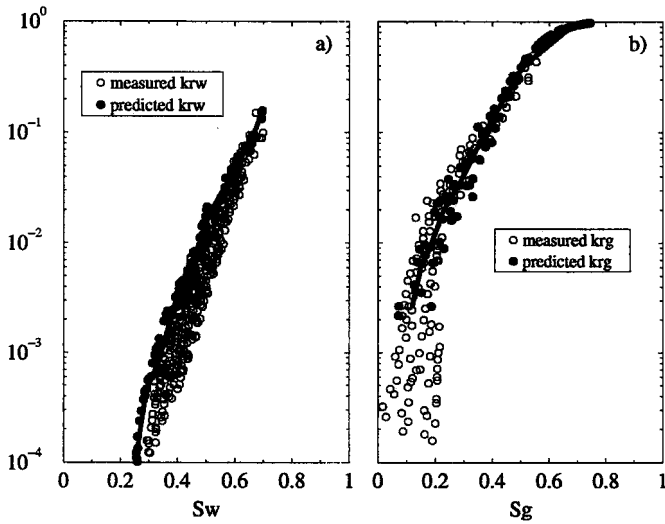
Fig. 9 – Predicted vs. measured three-phase drainage relative permeabilities. (a) water, and (b) gas.

Fig. 10 – Predicted vs. measured three-phase drainage oil relative permeabilities.

Three-phase predictions. We complete the comparison between measured and predicted relative permeabilities of water wet Berea sandstone by presenting three-phase data in **Figs. 9 and 10**. To obtain our predictions, we simulated gas injection after primary drainage to various water saturations. Fig. 9 (a) shows that the predicted water relative permeabilities are in fair agreement with the experimental data. However, we seem to systematically over-predict the measured water permeabilities, especially at low water saturations. The reason for this discrepancy is not clear. The simulated two-phase and three-phase water relative permeabilities are almost identical. This is in agreement with the commonly accepted concept that water permeability in water wet media is the same in two-phase and three-phase flow, i.e. it is only a function of its own saturation.

Fig. 9 (b) displays the simulated drainage gas relative permeabilities. The agreement between predicted and measured data is excellent. Again, the finite size of our samples prohibits us from measuring non-zero gas relative permeability at very low gas saturations. The large spread in the experimental data at low gas saturations was reported to have resulted from experimental difficulties [25]. Similar to the water permeability, the simulated gas permeability in three-phase drainage is almost identical to that in two-phase drainage, i.e. gas permeability is largely insensitive to the saturation history.

Figure 10 displays measured and predicted three-phase oil relative permeabilities. Again, the predicted and measured permeabilities are in good agreement. This confirms the validity of the pore-scale displacement mechanisms on which the model is based. The scatter in the simulated data is similar to that of the experimental data. We note
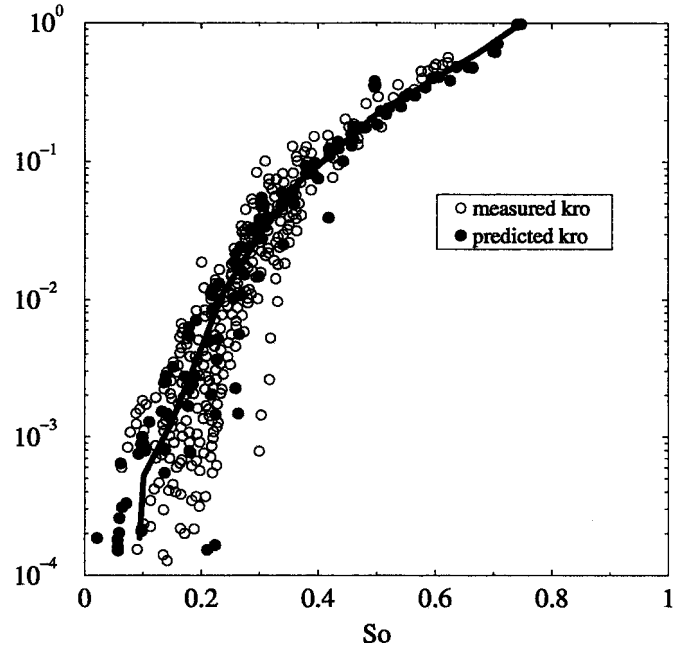
that the scatter for the oil permeability is significantly larger than that for the wetting and non-wetting phases. This clearly shows that oil permeabilities in three-phase flow are strongly dependent on the saturation history. For the three-phase drainage displacements considered here, this is mainly attributed to the fact that the stability of the oil layers depends critically on the oil-water capillary pressure at the commencement of the gas injection (i.e. the water saturation after primary drainage).

If R_{cow} is high (i.e. low water saturation), stable oil layers can exist until a large value of R_{cgo} is reached. In this case, oil layer drainage may allow very low oil saturation to be reached. If, on the other hand, R_{cow} is low (i.e. high water saturation), oil layers exist only for a short range of R_{cgo} and we expect limited oil layer drainage. In the absence of oil layers, oil can be trapped by both gas and water, leading to reduced oil recovery. For the simulated results, the residual oil saturation after gas flooding ranged roughly from 1% to 20%, depending on the initial water saturation. Consequently, both the oil permeability and the residual oil saturation depend strongly on the saturation history.

Although these preliminary results are quite encouraging, it is not known how accurately the three-phase network model can predict relative permeabilities for imbibition dominated three-phase flow and three-phase flow in mixed wet systems, such as those often encountered in oil reservoirs. This is currently being investigated and will be reported later.

Conclusion

Using standard petrographical thin section data for Berea sandstone, we:

1. Reconstructed 3D pore space samples which adequately reproduce important intrinsic properties of the actual sandstone such as correlation functions, local porosity distributions, and the degree of connectivity.

2. Calculated absolute permeability and formation factor by numerically solving the governing partial differential equations. Computed transport properties agree reasonably well with those of a microtomography image of Berea sandstone.

3. Accurately predicted two-phase drainage and imbibition relative permeabilities for Berea sandstone from pore-scale simulations on the reconstructed samples.

4. Successfully predicted gas, oil, and water relative permeabilities for drainage dominated three-phase flow in water wet Berea sandstone.

5. Simulated gas and water relative permeabilities for three-phase drainage are largely insensitive to the saturation history. Recovery and relative permeability of the intermediate oil phase are strongly dependent on the saturation history.

Acknowledgements

References

1. Stone, H.L.: 1970, "Probability Model for Estimating Three-Phase Relative Permeability", *J. Petrol. Tech.* **22**, 214–218.
2. Stone, H.L.: 1973, "Estimation of Three-Phase Relative Permeability and Residual Oil Data", *J. Canad. Petrol. Tech.* **12**, 53–61.
3. Baker, L.E.: 1988, "Three-Phase Relative Permeability Correlations", SPE 17369, proceedings of the SPE/DOE Symposium on Enhanced Oil Recovery, Tulsa, OK, April 17-20.
4. Parker, J.C. and Lenhard, R.J.: 1990, "Determining Three-Phase Permeability-Saturation-Pressure Relations from Two-Phase Measurements", *J. Petrol. Sci. Eng.* **4**, 57–65.
5. Hustad, O.S. and Hansen, A.G.: 1995, "A Consistent Correlation for Three-Phase Relative Permeabilities and Phase Pressures based on Three Sets of Two-phase Data", proceedings of the Eight European Symposium on Improved Oil Recovery, Vienna, May 15-17.

6. Blunt M.J.: 1999, "An Empirical Model for Three-Phase Relative Permeability", SPE 56474, Proceedings of the SPE Annual Technical Conference and Exhibition, Houston, TX, October 3-6.
7. Kantzas, A., Chatziz, I., and Dullien, F.A.L.: 1988, "Enhanced Oil Recovery by Inert Gas Injection", SPE 13264, Proceedings of the Sixth SPE/DOE Symposium on Enhanced Oil Recovery, Tulsa, OK, April 1988.
8. Øren, P.E. and Pinczewski, W.V.: 1992, "Mobilization of Waterflood Residual Oil by Gas Injection for Water Wet Conditions", *SPE Formation Evaluation'* **7**, 70–78.
9. Øren, P.E. and Pinczewski, W.V.: 1994, "Effect of Wettability and Spreading on Recovery of Waterflood Residual Oil by Immiscible Gasflooding", *SPE Formation Evaluation'* **9**, 149–156.
10. Øren, P.E. and Pinczewski, W.V.: 1995, "Fluid Distribution and Pore-Scale Displacement Mechanisms in Drainage Dominated Three-Phase Flow", *Transport in Porous Media* **20**, 105–133.
11. Blunt, M., Zhou, D., and Fenwick, D.: 1995, "Three-Phase Flow and Gravity Drainage in Porous Media", *Transport in Porous Media* **20**, 77–103.
12. Soll, W.E., Celia, M.A., and Wilson, J.L.: 1993, "Micromodel Studies of Three-Fluid Porous Media Systems: Pore-Scale Processes Relating to Capillary Pressure–Saturation Relationships", *Water Resources Research* **29**, 2963–2974.
13. Dong, M., Dullien, F.A.L., and Chatziz, I.: 1995, "Imbibition of Oil in Film Form over Water Present in Edges of Capillaries with Angular Cross-Section", *J. Coll. & Interf. Sci.* **172**, 278–288.
14. Vizika, O. and Lombard, J.M.: 1996, "Wettability and Spreading: Two Key Parameters in Oil Recovery with Three-Phase Gravity Drainage", *SPE Reservoir Engineering* **11**, 54–60.
15. Keller, A.A., Blunt, M.J., and Roberts, P.V.: 1997, "Micromodel Observation of the Role of Oil Layers in Three-Phase Flow", *Transport in Porous Media* **20**, 105–133.
16. Heiba, A.A., Davis, H.T., and Scriven, L.E.: 1984, "Statistical Network Theory of Three-Phase Relative Permeabilities", SPE 12690, Proceedings of the SPE/DOE Symposium on Enhanced Oil Recovery, Tulsa, OK, April 15-18.
17. Øren, P.E., Billiotte, J., and Pinczewski, W.V.: 1994, "Pore-Scale Network Modeling of Waterflood Residual Oil Recovery by Immiscible Gas Flooding", SPE/DOE 27814, Proceedings of the SPE/DOE Symposium on Enhanced Oil Recovery, Tulsa, OK, April 1994.
18. Pereira, G.G., Pinczewski, W.V., Chan, D.Y.C., Paterson, L., and Øren, P.E.: 1996, "Pore-Scale Network Model for Drainage Dominated Three-Phase Flow in Porous Media", *Transport in Porous Media* **24**, 167–201.
19. Fenwick, D.H. and Blunt M.J.: 1998a, "Network Modelling of Three-Phase Flow in Porous Media", *SPE Journal* **3**, 86–97.
20. Fenwick, D.H. and Blunt M.J.: 1998b, "Three-Dimensional Modeling of Three-Phase Imbibition and Drainage", *Advances in Water Resources* **25**, 121–143.
21. Mani, V. and Mohanty, K.K.: 1998, "Pore-Level Network

Modeling of Three-Phase Capillary Pressure and Relative Permeability Curves", *SPE Journal* **3**, 238–248.

22. Bakke, S., and Øren, P.E.: 1997, "3-D Pore-Scale Modelling of Sandstones and Flow Simulations in the Pore Network", *SPE Journal* **2**, 136–149.

23. Øren, P.E., and Bakke, S.: 2000, "Process Based Reconstruction of Sandstones and Prediction of Transport Properties", Proceedings of Upscaling Downunder, Melbourne, Austalia, February 2000.

24. Øren, P.E., Bakke, S., and Arntzen, O.J.: 1998, "Extending Predictive Capabilities to Network Models", *SPE Journal* **3**, 324–336.

25. Oak, M.J.: 1990, "Three-Phase Relative Permeability of Water-Wet Berea", SPE/DOE 20183, Proceeding of the SPE/DOE Symposium on Enhanced Oil Recovery, Tulsa, OK, April 1990.

26. Churcher, L., and French, P.R., and Shaw, J.C., and Schramm, L.L.: 1991, "Rock Properties of Berea Sandstone, Baker Dolomite, and Indiana Limestone", SPE 21044, Proceedings of the SPE International Symposium on Oilfield Chemistry, Anaheim, CA, February 20-22.

27. Hazlett, R.D.: 1997, "Statistical Characterization and Stochastic Modeling of Pore Networks in Relation to Fluid Flow", *Math. Geol.* **29**, 801–822.

28. Adler, P.M., Jacquin, C.G., and Quiblier, J.A.: 1990, "Flow in Simulated Porous Media", *Int. J. Multiphase Flow* **16**, 691–712.

29. Roberts, A.P.: 1997, "Statistical reconstruction of three-dimensional porous media from two-dimensional images", *Physical Reveiw E* **56**, 3203–3212.

30. Yeong, C.L.Y. and Torquato, S.: 1998, "Reconstructing Random Media II. Three-Dimensional Media from Two-Dimensional Cuts", *Physical Review E* **58**, 224–233.

31. Hilfer, R.: 1991, "Geometric and Dielectric Characterization of Porous Media", *Physical Review B* **44**, 60–75.

32. Hilfer, R.: 1996, "Transport and Relaxation Phenomena in Porous Media", *Advances in Chemical Physics* **92**, 299–424.

33. Biswal, B., Manwarth, C., and Hilfer, R.: 1998, "Three-dimensional Local Porosity Analysis of Porous Media", *Physica A* **225**, 221–241.

34. Biswal, B., Manwarth, C., Hilfer, R., Bakke S., and Øren, P.E.: 1999, "Quantitative Analysis of Experimental and Synthetic Microstructures for Sedimentary Rocks", *Physica A* **273**, 452–475.

35. Peyret, R. and Taylor, T.D,: 1983, "Computational Methods for Fluid Flow", Springer Verlag, New York.

36. Ferreol, B. and Rothman, D.H.: 1995, "Lattice-Boltzmann Simulations of Flow through Porous Media", *Transport in Porous Media* **20**, 3–20.

37. Ranshoff, T.C. and Radke, C.J.: 1988, "Laminar Flow of Wetting Liquid along the Corners of a Predominatly Gas-Occupied Noncircular Pore", *J. of Colloid and Interface Science* **121**, 392–401.

38. Fenwick D.H. and Blunt, M.J.: 1995, "Pore Level Modelling of Three-Phase Flow in Porous Media", Proceedings of the 8th European IOR Sympoisum, Vienna, Austria, May 15-17.

39. Hjelmeland, O., Selle, O.M., and Rueslåtten, H.: 1987, "The Effects of Rock Properties on Wettability of Oil Reservoirs – An Investigation of North Sea Systems", Proceedings of the European Symposium on Enhanced Oil Recovery, Hamburg, Germany, October 27-29.